nature electronics

Article

https://doi.org/10.1038/s41928-023-00978-0

Electrically tunable moiré magnetism in twisted double bilayers of chromium triiodide

Received: 29 April 2022

Accepted: 16 May 2023

Published online: 19 June 2023

Check for updates

Guanghui Cheng[1,2,3,4,13], Mohammad Mushfiqur Rahman[5,13], Andres Llacsahuanga Allcca[1,2,6], Avinash Rustagi[5,12], Xingtao Liu[1,7], Lina Liu[1,2], Lei Fu[1,2], Yanglin Zhu[8], Zhiqiang Mao[8], Kenji Watanabe[9], Takashi Taniguchi[10], Pramey Upadhyaya[2,5,6] ✉ & Yong P. Chen[1,2,4,5,6,11] ✉

Moiré superlattices in van der Waals structures can be used to control the electronic properties of the material and can lead to emergent correlated and topological phenomena. Non-collinear states and domain structures have previously been observed in twisted van der Waals magnets, but the effective manipulation of the magnetic behaviour remains challenging. Here we report electrically tunable moiré magnetism in twisted double bilayers—that is, a bilayer plus a bilayer with a twist angle between them—of layered antiferromagnet chromium triiodide. Using magneto-optical Kerr effect microscopy, we observe the coexistence of antiferromagnetic and ferromagnetic order with non-zero net magnetization—a hallmark of moiré magnetism. Such a magnetic state extends over a wide range of twist angles (with transitions at around 0° and above 20°) and exhibits a non-monotonic temperature dependence. We also demonstrate voltage-assisted magnetic switching. The observed non-trivial magnetic states, as well as control via twist angle, temperature and electrical gating, are supported by a simulated phase diagram of moiré magnetism.

Moiré superlattices are created by stacking one layer of a van der Waals (vdW) material onto another layer with either a lattice mismatch or a small twist angle[1–13]. Such large superperiodic patterns define a new crystal structure with electronic bands folded into a mini-Brillouin zone, which can form flat bands and can drive the system into strongly correlated regimes. Due to the control they offer over the charge degree of freedom, moiré superlattices are a versatile electronic quantum simulator and platform to discover new phases of matter. A range of properties—including superconductivity, Mott insulating states and moiré excitons—have been observed in twisted graphene, transition metal dichalcogenides and other electronic materials[1–6,8,13].

[1]Department of Physics and Astronomy, and Birck Nanotechnology Center, Purdue University, West Lafayette, IN, USA. [2]Purdue Quantum Science and Engineering Institute, Purdue University, West Lafayette, IN, USA. [3]Department of Physics, University of Science and Technology of China, Hefei, China. [4]WPI-AIMR International Research Center for Materials Sciences, Tohoku University, Sendai, Japan. [5]Elmore Family School of Electrical and Computer Engineering, Purdue University, West Lafayette, IN, USA. [6]Quantum Science Center, Oak Ridge, TN, USA. [7]School of Industrial Engineering, Purdue University, West Lafayette, IN, USA. [8]Department of Physics, Pennsylvania State University, University Park, PA, USA. [9]Research Center for Functional Materials, National Institute for Materials Science, Tsukuba, Japan. [10]International Center for Materials Nanoarchitectonics, National Institute for Materials Science, Tsukuba, Japan. [11]Institute of Physics and Astronomy and Villum Centers for Dirac Materials and for Hybrid Quantum Materials, Aarhus University, Aarhus-C, Denmark. [12]Present address: Intel Corp., Hillsboro, OR, USA. [13]These authors contributed equally: Guanghui Cheng, Mohammad Mushfiqur Rahman. ✉e-mail: prameyup@purdue.edu; yongchen@purdue.edu

https://doi.org/10.1038/s41928-023-00978-0

VdW magnets exhibit two-dimensional magnetic phenomena and can be used to manipulate the spin degree of freedom[14–20]. Theoretical analyses have predicted that the twisted bilayers of vdW magnets can host exotic magnetic phases[21–24], suggesting, in particular, that non-collinear spin textures, topological skyrmion lattices and rich spectra of magnonic sub-bands can emerge from the modulation of interlayer exchange interactions[21–24].

The layered antiferromagnet chromium triiodide (CrI_3) is of potential interest in this regard. The interlayer magnetic exchange of bilayer CrI_3 depends on the structural stacking order[18,25]: monoclinic stacking favouring antiferromagnetic (AFM) coupling (as in "natural" bilayers, with zero net magnetization) and rhombohedral stacking favouring ferromagnetic (FM) coupling. Twisting one CrI_3 layer relative to another layer can create a moiré superlattice with rhombus-shaped primitive cells (Fig. 1a). The atomic registry varies continuously, leading to alternating structural domains such as AA stacking (top and bottom Cr atoms are vertically aligned), rhombohedral stacking and monoclinic stacking. Therefore, the stacking-dependent interlayer exchange in twisted CrI_3 can give rise to magnetic domains and non-collinear spin textures.

Such coexisting AFM and FM states have recently been experimentally demonstrated in twisted CrI_3 using magneto-optical measurements and Raman spectroscopy[11,12], and the nanoscale magnetic domains have been visualized with quantum magnetometry[10]. These discoveries highlight twisted vdW magnets as potential platforms to explore and engineer non-trivial magnetic phases. However, the effective manipulation of moiré magnetism—including magnetization reversal using electrical methods—remains challenging[17,26,27].

In this article, we report electrically tunable moiré magnetism in twisted double bilayer (tDB) CrI_3 (that is, a bilayer plus a bilayer with a twist angle between them). We show that the coexistence of AFM and FM orders can be tuned by the twist angle. We also observe a non-monotonic temperature dependence of magnetization and demonstrate electrical control over the magnetic states. Our experimental observations are supported by theoretical analysis, and we develop a phase diagram of moiré magnetism in the tDB system, which hosts a rich class of non-collinear states beyond those observed in twisted bilayer (single layer plus single layer) magnets[10,11] due to the increased layer degree of freedom.

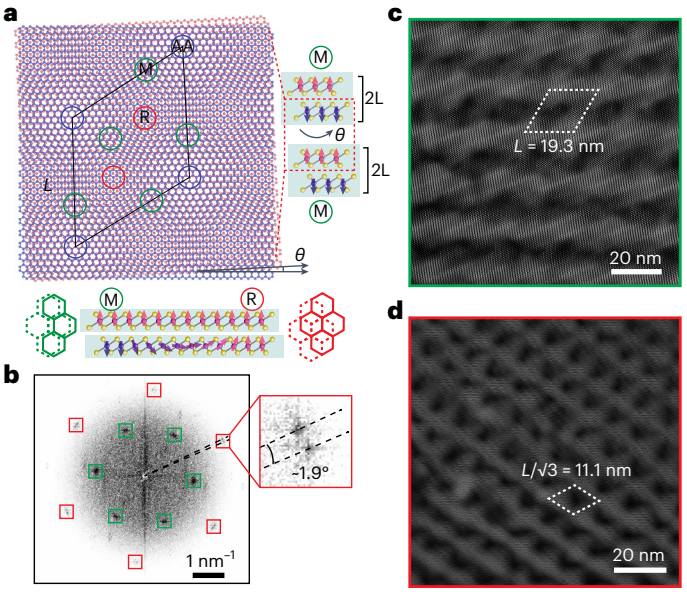

Fig. 1 | Moiré superlattice and STEM characterizations of tDB CrI_3. a, Moiré superlattice structure of tDB CrI_3 with a twist angle θ between the two bilayers. Only Cr atoms of the middle two CrI_3 layers are shown for simplicity, with the red and blue balls belonging to each of the two layers. Regions of AA stacking, monoclinic (M) stacking and rhombohedral (R) stacking are indicated by blue, green and red circles, respectively. The rhombus-shaped lines indicate the moiré primitive cell with a period of L. The middle two layers of tDB CrI_3 are twisted, and the top/bottom CrI_3 bilayers (2L) retain the monoclinic stacking (right). Non-collinear spin textures of the monoclinic–rhombohedral DW formed in the twisted middle two layers (bottom). **b**, FFT pattern of the STEM image (Supplementary Fig. 2) of a tDB CrI_3 with a target twist angle of 1.42°. The green and red rectangles mark the first- and second-order Bragg peaks, respectively. The magnification of one peak shows two slightly separated peaks from the top and bottom bilayer CrI_3 with a measured twist angle of around 1.9°(±0.3°) (right). **c**,**d**, Real-space moiré patterns reconstructed by the inverse FFT of the two sets of Bragg peaks marked by the green and red rectangles in **b**. The rhombus-shaped lines indicate primitive cells with periods related to moiré wavelength L.

Moiré superlattice of tDB CrI_3

We fabricated tDB CrI_3 by the tear-and-stack technique[13,28] in an argon glovebox and encapsulated it with hexagonal boron nitride (hBN) flakes (Methods). The atomic force microscopy image (Supplementary Fig. 1) suggests a uniform stacking interface with few bubbles. We employ magneto-optical Kerr effect (MOKE) microscopy under a polar configuration as the primary measurement due to its high sensitivity to magnetic moments perpendicular to the sample surface[29]. All the MOKE measurements were performed under a perpendicular magnetic field at a temperature of 6 K, unless otherwise specified (Methods).

We use high-angle annular dark-field scanning transmission electron microscopy (STEM) to characterize the moiré superlattice of tDB CrI_3 (Methods). Figure 1b shows the fast Fourier transform (FFT) of the STEM image of a tDB CrI_3 with a target twist angle of 1.42° (Supplementary Fig. 2 shows the original STEM images). Two sets of first- and second-order Bragg peaks with six-fold rotation symmetry are marked by the green and red rectangles, respectively, in Fig. 1b. A close inspection of one representative peak shows two slightly separated peaks corresponding to the top and bottom bilayer CrI_3. As a comparison, no splitting is observed for the Bragg peaks of the natural bilayer CrI_3 (Supplementary Fig. 2). From the splitting, we can measure the actual twist angle to be ~1.9°, within the accuracy of approximately ±0.5° of the stacking processes. Such twist angle accuracy is comparable with that in other works[10–12]. In this paper, unless otherwise specified, all the twist angles (denoted by θ) of the experimental samples refer to the target twist angles. The moiré wavelength[30] can be estimated to be $L = \frac{a}{2\sin(\theta/2)}$, where a is the lattice constant of CrI_3 (ref. 24) and is ~20.5 nm for the above sample. By inverse FFT of the two sets of Bragg peaks marked by the green and red rectangles (Fig. 1b), the real-space moiré patterns are reconstructed in Fig. 1c,d, corresponding to the first and second orders of the moiré superlattice. Both pattern periods are consistent with the expectations L and $L/\sqrt{3}$ based on the moiré wavelength. The STEM characterizations demonstrate the formation of a moiré superlattice in tDB CrI_3.

Twist angle and temperature dependence of magnetism

Figure 2a shows the optical micrographs of a representative bilayer CrI_3 flake (left) and a 5°-tDB CrI_3 (right) made from it. The MOKE signals as a function of magnetic field in bilayer CrI_3 and 5°-tDB CrI_3 are shown in Fig. 2b,c, measured at the yellow and red spots shown in Fig. 2a, respectively. In the bilayer CrI_3 region, we observed zero magnetization at zero field and sharp jumps at fields of approximately ±0.7 T, consistent with the reported AFM spin-flip transition in natural bilayer CrI_3 (refs. 31,32). The magnetic ground states are shown in the insets in Fig. 2b.

Within the tDB CrI_3 region, in addition to the AFM spin-flip transitions present at fields of approximately ±0.7 T (since these are analogous to the transitions observed in bilayer CrI_3, we refer to them as 'AFM spin-flip transitions' hereafter even for the tDB system), an FM hysteresis loop emerges with transition fields of approximately ±0.2 T.

https://doi.org/10.1038/s41928-023-00978-0

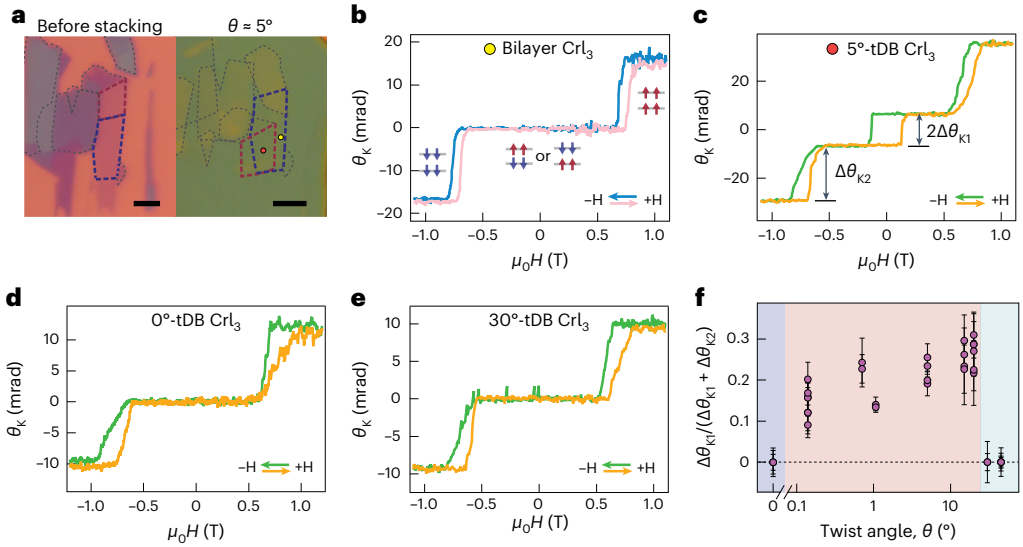

Fig. 2 | Twist angle dependence of the magnetism in tDB CrI_3. a, Optical micrographs of a bilayer CrI_3 flake (left) and a 5°-tDB CrI_3 (right) made from it by the tear-and-stack technique. The top and bottom bilayers of CrI_3 are outlined by the blue and red dashed lines, respectively. The thicker flakes are outlined by the grey dashed lines. Scale bars, 5 μm. **b**,**c**, MOKE signal as a function of perpendicular magnetic field in bilayer CrI_3 (**b**) and 5°-tDB CrI_3 (**c**) (both from the same CrI_3 flake), measured at the yellow and red spots in **a**, respectively. Magnitudes of the FM loop and AFM spin-flip transition are denoted by $\Delta\theta_{K1}$ and $\Delta\theta_{K2}$. The insets in **b** depict the magnetic ground states of bilayer CrI_3. The potential spin orientations in each layer for **c** are shown in Supplementary Fig. 16. **d**,**e**, MOKE signal as a function of magnetic field in 0°-tDB CrI_3 (**d**) and 30°-tDB CrI_3 (**e**). **f**, Fraction of MOKE magnitudes $\Delta\theta_{K1}/(\Delta\theta_{K1} + \Delta\theta_{K2})$ as a function of the twist angle (θ, in the log scale). The data points at each angle are measured at different positions of each sample. Data (zero value) at θ of 0°, 30° and 45° have at least two reproducible points overlapping. The blue-, pink- and cyan-shaded areas are guides to the eyes. The twist angle accuracy is around 0.5°. The error bars are the uncertainties in extracting the MOKE magnitudes, including the difference between the forward and backward sweeps of the magnetic field and the standard deviation.

In comparison, the MOKE results of natural four-layer CrI_3 suggest interlayer AFM coupling without an FM loop[32] (Supplementary Fig. 3). For tDB CrI_3, the assumption of interlayer AFM spin orientations within each of the top and bottom bilayers breaks down, since it leads to zero net magnetization regardless of the coupling type between the middle two layers. Here we propose that the observed AFM and FM behaviours in tDB CrI_3 are due to the coexistence of AFM/FM domains predicted for moiré magnetism[21,23]. Although a similar coexistence of magnetic domains has been reported in twisted bilayer CrI_3 (refs. 10–12), our tDBs have the potential to support a richer magnetic phase diagram and behaviours, as discussed later.

The moiré magnetism is determined by competing magnetic interactions dependent on the twist angle[21,24]. We, thus, studied the twist angle dependence of the magnetic behaviours in tDB CrI_3. Figure 2d,e shows the MOKE results in 0°- and 30°-tDB CrI_3, respectively (0°-tDB CrI_3 refers to stacking bilayer on bilayer with 0°, instead of a natural four-layer CrI_3). Only AFM spin-flip transitions are present, whereas the FM loop disappears, in contrast to 5°-tDB CrI_3. Supplementary Fig. 4 shows data from other samples with additional twist angles. Furthermore, the MOKE results of a representative tDB CrI_3 sample exhibiting both FM loop and AFM spin-flip transitions show no other transitions up to higher fields of ±2 T (Supplementary Fig. 5).

We refer to the magnitudes of the FM loop and AFM spin-flip transition as $\Delta\theta_{K1}$ and $\Delta\theta_{K2}$, respectively, and summarize the phenomenological 'FM fraction' as $\Delta\theta_{K1}/(\Delta\theta_{K1} + \Delta\theta_{K2})$ as a function of the twist angle (Fig. 2f). The data points at each twist angle are obtained at different positions in each sample (Supplementary Fig. 6 shows the uniformity check). The non-zero fractions (reaching a maximum value of ~0.3) in the twist angle ranging from 0.14° to 20.00° indicate a regime with coexisting FM and AFM. The FM loop disappears for twist angles of ~0° or above 20°, suggesting phase transitions across critical angles. Such systematic twist angle dependence and reproducible results support the non-collinear moiré magnetism emerging in tDB CrI_3. The possible non-collinear phases will be discussed with the theoretically calculated phase diagram shown later. We further plot another quantity—the transition fields of both FM coercivity and AFM spin flip—as a function of the twist angle (Supplementary Fig. 7). No substantial dependence is observed, suggesting that the magnetic anisotropy in this system is hardly tuned by the moiré superlattice. We note that compared with other recent measurements in the tDB CrI_3 system[12,33], the magnetic transitions appear sharper in our MOKE curves, possibly related to the background subtraction in our MOKE signal and disorder-dependent coercivity[34].

We further investigate the temperature dependence of the magnetic behaviours. Figure 3a,b shows the MOKE results for bilayer CrI_3 and 0.71°-tDB CrI_3 at various temperatures. With increasing temperature, the FM coercivity and AFM spin-flip transitions occur at lower fields and with reduced MOKE amplitudes (except for the anomalous non-monotonic behaviour of the FM loop amplitude for tDB CrI_3, as discussed later), eventually disappearing at ~40–50 K, consistent with the studies in natural bilayer CrI_3 and twisted bilayer CrI_3 (refs. 11,17,31). The critical temperature of FM coercivity is higher than that of the AFM spin-flip transition, possibly because the two transitions (AFM versus FM) correspond to spin reorientation involving different regions and different types of coupling of the tDB system (Supplementary Figs. 13–16 provide the expected spin reorientations corresponding to these transitions); consequently, the coercivities and net change in magnetization corresponding to these transitions are controlled by different material parameters, possibly giving rise to different critical temperatures.

Figure 3c shows the MOKE magnitudes of the AFM spin-flip transition $\Delta\theta_{K0}$ in the natural bilayer, as well as the FM loop $\Delta\theta_{K1}$, AFM spin-flip transition $\Delta\theta_{K2}$ and total magnitude $\Delta\theta_{K1} + \Delta\theta_{K2}$ in tDB, as functions of temperature extracted from Fig. 3a,b. Remarkably, $\Delta\theta_{K1}$ of 0.71°-tDB CrI_3 (proportional to the net out-of-plane magnetization within the non-collinear phase) first increases and then decreases with increasing

https://doi.org/10.1038/s41928-023-00978-0

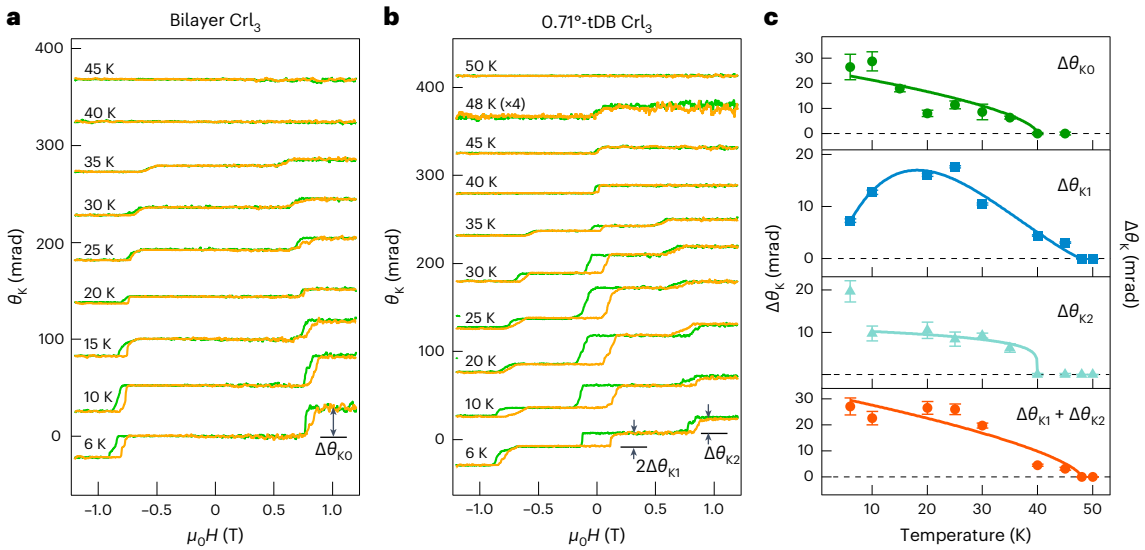

Fig. 3 | Temperature dependence of the magnetism in tDB CrI_3. a,**b**, MOKE signal as a function of magnetic field at representative temperatures in bilayer CrI_3 (**a**) and 0.71°-tDB CrI_3 (from the same bilayer CrI_3 flake) (**b**). The curves are vertically shifted for clarity. The data at 48 K are scaled by a factor of four for better comparison. **c**, MOKE magnitudes of the bilayer AFM spin-flip transition $\Delta\theta_{K0}$, the tDB FM loop $\Delta\theta_{K1}$, the AFM spin-flip transition $\Delta\theta_{K2}$ and the total magnitude $\Delta\theta_{K1} + \Delta\theta_{K2}$ as functions of temperature. All the values are extracted from MOKE results in bilayer CrI_3 sample and tDB CrI_3 sample, as shown in **a** and **b**. The solid lines are phenomenological fits with the power-law form, as guides to the eyes. The error bars are the uncertainties in extracting the MOKE magnitudes, including the difference between the forward and backward sweeps of the magnetic field and standard deviation.

temperature. In contrast, $\Delta\theta_{K0}$ of bilayer CrI_3 and $\Delta\theta_{K2}$ and $\Delta\theta_{K1} + \Delta\theta_{K2}$ of 0.71°-tDB CrI_3 (proportional to the saturation magnetization of the sample, M_s) monotonically decrease with increasing temperature, typical of magnets making a transition from an FM phase to a paramagnetic phase. Supplementary Fig. 8 presents additional examples of such a non-monotonic temperature dependence of $\Delta\theta_{K1}$ observed in another tDB CrI_3 sample. As discussed below, such anomalous non-monotonic behaviour of $\Delta\theta_{K1}$ is further consistent with the presence of non-collinear phases predicted in this system. It can be qualitatively understood as the temperature-induced crossover between non-collinear phases arising from different power-law dependences of the magnetic parameters (anisotropy K, interlayer exchange $J_\perp^0$ and intralayer exchange A) with temperature[11,35,36].

Electrical control of magnetism

We next explore the electrical control of the magnetic behaviours in tDB CrI_3. We fabricated a back-gated 0.14°-tDB CrI_3 device (Methods) (Fig. 4a,b). The MOKE results at a gate voltage of −80 V (Fig. 4c) show the coexistence of AFM and FM transitions, the same feature as discussed above for non-collinear moiré magnetism. Four plateaus at low fields representing distinct magnetic states are denoted by A, B, C and D (having positive, negative, negative and positive magnetization, respectively, with the MOKE signal sign consistent with the correspondingly polarized state at high fields). Figure 4d shows the MOKE signal as a function of the magnetic field at various back-gate voltages (Supplementary Fig. 9 shows the representative MOKE curves). The top and bottom panels in Fig. 4d correspond to backward and forward sweeps of the magnetic field, respectively. The sharp colour boundaries represent FM coercivity and AFM spin-flip transitions. Both occur at lower magnetic fields with increasing back-gate voltage, suggesting the high electrical tunability of magnetic anisotropy and interlayer exchange. Similar electrical tunability is observed in natural bilayer CrI_3 (refs. 17,27,37), which is associated with doping-modulated interlayer exchange coupling.

We also observed voltage-controlled magnetic switching in tDB CrI_3. Such switching is essentially due to the electrical modulation of coercive fields. Here we biased the magnetic field close to the FM coercive fields denoted by the circled numbers in Fig. 4c. The corresponding MOKE signal as a function of back-gate voltage V_{bg} is shown in Fig. 4e. At a fixed voltage $V_{bg} = -80$ V, the tDB CrI_3 sample is first initialized by applying a high magnetic field of 1.000 T and then biased at a field of −0.141 T (trace 1), corresponding to a non-collinear ground state (A state, with positive magnetization). When sweeping V_{bg} from −80 to 80 V, an abrupt switching to the B state occurs at approximately 70 V. For biased fields of −0.151 T (trace 2) and −0.160 T (trace 3), which are still higher but closer to the coercive field (−0.178 T) at $V_{bg} = -80$ V, switching occurs at earlier voltages of −10 and −50 V, respectively. This is consistent with the trend of decreasing coercive field magnitude for more positive V_{bg} (Fig. 4d and Supplementary Fig. 9) for this sample. However, the system stays at the B state when sweeping the voltage backwards, presumably because the B state with negative magnetization is the low-energy state under the negative magnetic field, and an energy barrier prevents the system from returning to the A state. Such one-time magnetic switching has also been reported in other FM systems[27,38]. After initialization by a negative high field of −1.000 T and biased fields of 0.140, 0.150 and 0.153 T (traces 4, 5 and 6, respectively, increasingly close to the coercive field of 0.174 T at $V_{bg} = -80$ V for the forward magnetic-field sweep), voltage-controlled switching is observed from a non-collinear state with negative magnetization (C state) to a state with positive magnetization (D state). The voltage-assisted switching is also observed in other tDB CrI_3 samples with twist angles of 5° and 20° (Supplementary Fig. 10).

In addition to voltage-assisted switching, we further observed a linear dependence of the MOKE signal on the voltage with a positive slope for traces 1, 2 and 3 (Fig. 4e). This suggests an increase in net magnetization (before switching occurs) as a function of gate voltage (this is true for the backward gate-voltage sweep, too, where magnetization becomes increasingly negative). When the magnetic field/magnetization is reversed (traces 4, 5 and 6), the magnetization versus voltage shows the opposite slope, but the net magnetization (before switching) still generally increases during voltage sweeps. Such linear dependences were also measured in two other samples (5°- and 20°-tDB; Supplementary Fig. 10), but the sign of the slope was opposite in the latter sample (20°-tDB, with generally decreasing magnetization magnitudes

https://doi.org/10.1038/s41928-023-00978-0

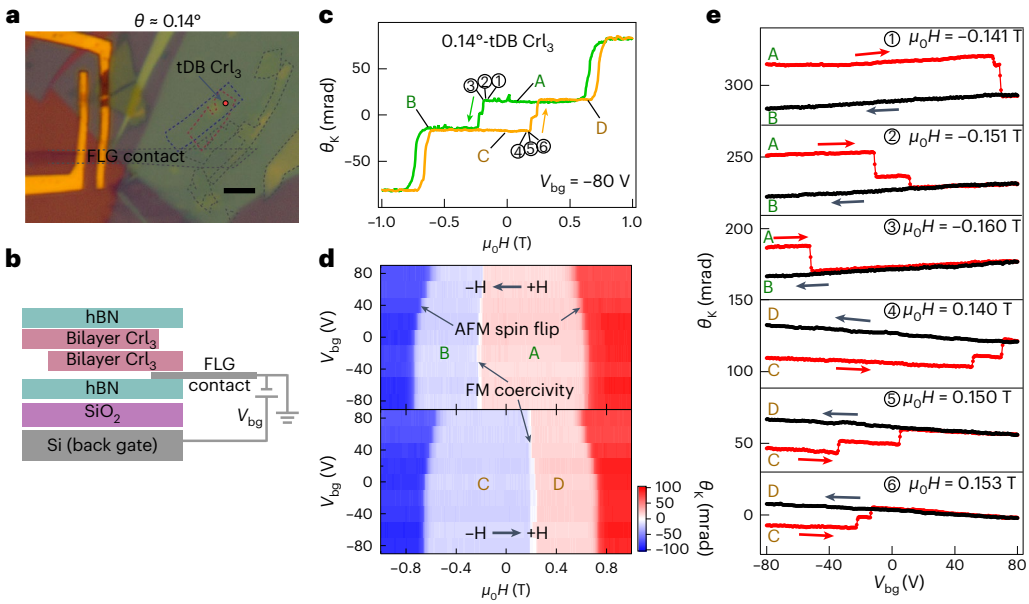

Fig. 4 | Electrical control of magnetism in tDB CrI_3. **a**,**b**, Optical micrograph (θ around 0.14°) (**a**) and schematic of the side view of a tDB CrI_3 device with a back-gate voltage V_{bg} applied (**b**). A few-layer graphene (FLG) flake is used as the contact to the stack. Scale bar, 5 μm. **c**, MOKE signal as a function of magnetic field at a gate voltage of −80 V. The field-sweeping directions are denoted by the arrows. Four plateaus at low fields are denoted by A, B, C and D. **d**, MOKE signal as a function of magnetic field and back-gate voltage V_{bg}. The top and bottom panels correspond to backward and forward sweeps of the magnetic field, respectively. The sharp colour boundaries marked by the arrows indicate the FM coercivity and AFM spin-flip transitions. **e**, Gate-voltage-controlled magnetic switching. Voltage-sweeping directions are denoted by the arrows. The sample is initialized by high magnetic fields of +(−)1 T and then biased at fields of ① −0.141 T, ② −0.151 T and ③ −0.160 T (④ 0.140 T, ⑤ 0.150 T and ⑥ 0.153 T, respectively), corresponding to the circled numbers in **c**. The intermediate states (minor plateaus) seen in **c** and **e** during A-to-B and C-to-D switching may be due to DW motion with pinning effect by defects[34,36].

during voltage sweeps; Supplementary Fig. 10f). These behaviours in response to voltage demonstrate an intriguing electrical tuning of distinct time-reversal states (A and B states versus C and D states) in tDB CrI_3 as a result of different samples and initialization processes. The observed gate-tunable magnetism may have two possible origins. The electrostatic field can break the spatial-inversion symmetry of the layered magnet and create layer polarization of spin carriers[17,37,39]. Furthermore, the gate voltage can effectively change the magnetic parameters of CrI_3 by electrostatic doping[27,40], which could change the location of the system on the phase diagram below (Fig. 5) and hence modulate magnetization in the twisted bilayers. We note that different slopes observed for different samples could arise because they are at different locations and have different (voltage-swept) trajectories in the parameter space and phase diagram (Supplementary Note 11). The observed electrical tunability allows us to access and control the non-collinear magnetic states in tDB CrI_3.

Theoretical analysis of moiré magnetism

To better understand the observations, we theoretically study the moiré magnetism in tDB CrI_3. Within the continuum approximation[21], the free energy per unit area for tDB CrI_3 with a relative twist between the middle two layers can be written as

$$\mathcal{F}(\vec{m}_1,\vec{m}_2,\vec{m}_3,\vec{m}_4) = A\sum_{i=1}^{4}(\nabla\vec{m}_i)^2$$
$$-K\sum_{i=1}^{4}m_{iz}^2 + J_\perp^0[\vec{m}_1\cdot\vec{m}_2 + \Phi(\vec{r})\vec{m}_2\cdot\vec{m}_3 + \vec{m}_3\cdot\vec{m}_4],$$

where $\vec{m}_i$ is the position ($\vec{r}$)-dependent unit vector oriented along the magnetization of layer i, A is the intralayer exchange stiffness, $K>0$ is the easy-axis anisotropy and $J_\perp^0$ is the interlayer exchange constant for monoclinic stacking. Here $\Phi(\vec{r})$ accounts for the spatially dependent interlayer exchange due to local variation in stacking between the twisted layers, acting as a new degree of freedom tunable via the twist angle. The relative strengths of the intralayer exchange, interlayer exchange and anisotropy energies determine the magnetic ground state of the system. Following the framework from another work[21], we define two dimensionless parameters, namely, $\alpha \equiv \frac{J_\perp^0}{Aq_m^2}$ and $\beta \equiv \frac{K}{Aq_m^2}$, that capture the relative strengths between these energy contributions, where $q_m = 1/L$ is the moiré wavevector.

Because of the increased 'layer degree of freedom' of the tDB system, a richer set of magnetic configurations beyond the twisted bilayer case[10–12,21,24] is necessary to characterize the possible ground states of our system as functions of α and β. We schematically depict them in Fig. 5a (for convenience, we label the layers from bottom to top as 1, 2, 3 and 4, and do not show the copies obtained by (1) time reversal or (2) simultaneous swapping of the spin configurations between layers 1↔4 and 2↔3 so that layers 1, 2, 3 and 4 are now from top to bottom). When the configurations are governed by minimizing the free-energy terms due to perpendicular anisotropy and interlayer exchange, the magnetization within each layer prefers to be primarily out of plane and have the interlayer spin orientations that minimize the local interlayer exchange (similar to the so-called twisted-A phase for twisted bilayer CrI_3; ref. 21). For tDB CrI_3, the resultant configuration harbours ~180° domain walls (DWs) in layers 1 and 2, which is referred to as twisted-A two domain walls (TA-2DW). On the other hand, when the intralayer exchange energy cost associated with these DWs becomes more important, the system can reduce energy by getting rid of the DW in one or both layers, giving rise to configurations referred to as twisted-A one domain wall (TA-1DW) and collinear states, respectively. Since the area fraction of the R-stacking and FM (interlayer coupling between layers 2 and 3) region per moiré cell is larger than that of the M-stacking and AFM region (Supplementary Fig. 11), and the maximum strengths of the interlayer exchange of the FM and AFM regions are approximately the same, FM orientations between layers 2 and 3 are favoured over AFM orientations for the

https://doi.org/10.1038/s41928-023-00978-0

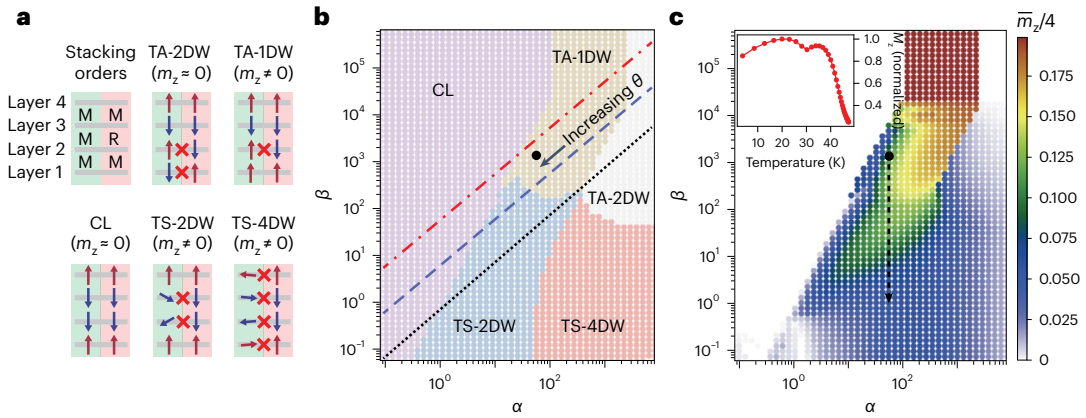

Fig. 5 | Theoretical analysis of the moiré magnetism in tDB CrI_3. a, Schematic of the magnetic phases: twisted-A phase two domain walls (TA-2DW), twisted-A phase one domain wall (TA-1DW), twisted-S phase two domain walls (TS-2DW), twisted-S phase four domain walls (TS-4DW) and collinear phase (CL, no DWs). Layers 1–4 are labelled from bottom to top. Monoclinic (M) and rhombohedral (R) stacking are labelled for each layer pair (sandwiching the label), and M/R regions between the middle two layers are indicated by green/pink colours. Out-of-plane (in-plane) spins in the four layers are denoted by vertical (horizontal) arrows. The red crosses denote the magnetic DWs where non-collinear spin textures exist. **b**, Magnetic phase diagram showing the emergence of non-collinear ground states as a function of dimensionless parameters α and β. The coloured dots denote the simulated cases. The red dot–dashed, blue dashed and black dotted lines correspond to constant $K/J_\perp^0$ ratios of 72.300, 7.230 and 0.723, respectively, suggesting phase transitions with the twist angle. **c**, Calculated net out-of-plane component of the dimensionless magnetization ($\overline{m_z}/4$) normalized by the value for fully spin-polarized states (such as out-of-plane spins ↑↑↑↑ in all the layers gives $\overline{m_z}/4 = 1$) as a function of α and β. The dashed arrow is an example trajectory of increasing temperature (T, starting from 7 K, with corresponding $(\alpha, \beta) = (56, 1{,}230)$ marked by the black dots in both **b** and **c**), giving a sharp drop in β and a non-monotonic behaviour of the overall out-of-plane physical magnetization M_z shown in the inset, for $\theta = 0.71°$.

collinear state. Finally, similar to the bilayer CrI_3 case, for weaker perpendicular anisotropy, magnetic configurations with substantial in-plane components (the so-called twisted-S phase[21]) can be favoured to lower the interlayer exchange energy via the formation of ~90° DWs (reducing DW widths compared with ~180° DWs). For tDB CrI_3, such ~90° DWs can be formed in the middle two layers or all the layers, resulting in configurations labelled as twisted-S two domain walls (TS-2DW) and twisted-S four domain walls (TS-4DW), respectively. By comparing the free energies of the abovementioned configurations (Supplementary Note 11), we present the phase diagram of the ground states for the tDB CrI_3 system (Fig. 5b).

Observations of moiré magnetism

We next provide a qualitative understanding of the experimental observations and compare our results with recent observations of moiré magnetism. We begin by focusing on the twist angle dependence of MOKE. To this end, we show the trajectory of the corresponding magnetic phases traversed as twist angle θ is increased (Fig. 5b). The blue dashed line corresponds to a calculation based on K, A and $J_\perp^0$ values extracted from the untwisted CrI_3 system[41,42]. Since the MOKE signal is proportional to perpendicular magnetization (Fig. 5c), we also show the calculated net out-of-plane magnetization component ($\overline{m_z}/4$) for different phases. For very small θ (that is, large α and β), the TA-2DW state is the ground state. This is because the small θ implies the presence of large moiré domains (of size around $L \propto a/\theta$) with varying signs of interlayer exchange. The system, thus, prefers to minimize the energy cost within the domains (at the expense of incurring intralayer exchange and anisotropy energy costs in the DWs) by choosing primarily out-of-plane magnetizations with interlayer arrangements following the sign of local interlayer exchange. Similar to the natural four-layer CrI_3, the TA-2DW phase carries negligible out-of-plane magnetization (Fig. 5c), consistent with the observed zero MOKE signal around zero twist angle (Fig. 2). With increasing twist angle θ, the DW energy (which increases proportionally to L; refs. 11,21) becomes comparable with the domain energy (which scales as L^2); the system, thus, transitions into the TA-1DW state, which, crucially, has a non-zero out-of-plane magnetization. Therefore, the observed MOKE signal going from 0 to finite values is consistent with the appearance of the TA-1DW state. As θ increases further, the cost of forming DWs becomes too high and the system eventually collapses into a collinear phase with no DWs and vanishing net out-of-plane magnetization. This transition leads to a drop in the MOKE signal back to zero (Fig. 2).

Based on the above discussion, we conclude that the TA-1DW state should be the most probable candidate to cause the emergent FM loops experimentally observed for intermediate twist angles (the anticipated magnetic field evolution of the TA-1DW state under various scenarios is further consistent with our experiments; Supplementary Figs. 13–16). We note, however, that lattice relaxation and/or disorder in the tDB system can effectively renormalize the material parameters. This can give rise to twist-angle-dependent trajectories different from the one followed for typical material parameters extracted from the untwisted CrI_3 system. To account for this variation, we also show ten times larger and smaller values of the ratio $K/J_\perp^0$ (Fig. 5b, red dot–dashed and black dotted lines, respectively). We notice that for smaller $K/J_\perp^0$, the system can traverse through the twisted-S phases, which also carry a non-zero out-of-plane magnetization. However, to experimentally observe the presence of such non-collinear phases in future research, other probes that are sensitive to in-plane magnetization are needed, such as longitudinal MOKE or spatially sensitive spin probes[10,43].

Using the phase diagram, we also provide a possible explanation for the observed anomalous temperature dependence of the MOKE signal (Fig. 3). In addition to the twist angle, the temperature dependence of the magnetic properties (K, $J_\perp^0$ and A) changes the relative strengths of the anisotropy, interlayer and intralayer exchange energies, resulting in a temperature-induced trajectory on the phase diagram. Depending on this trajectory and the starting phase, the overall out-of-plane physical magnetization ($M_z = \overline{m_z} M_s$) can increase with temperature before vanishing near the phase transition to the paramagnetic state. Here M_s is the saturation magnetization. To demonstrate this possibility, we choose the twist angle of $\theta = 0.71°$ (similar to the device shown in Fig. 3), starting from $(\alpha, \beta) = (56, 1{,}230)$ at low temperatures (the parameters were chosen between the red

dot–dashed and black dotted lines mentioned above), and track the evolution of the system on the phase diagram as the temperature is increased. To this end, we vary K, $J_{\perp}^{0}$, A and M_s according to the power law of temperature around $(1 - T/T_c)^{\gamma}$, where T_c is the Curie temperature, with exponents γ that were experimentally obtained to be around 2.300, 0.220, 0.220 and 0.125 (refs. 11,35,36). With increasing temperature (Fig. 5c, dashed arrow), $\overline{m}_z/4$ indeed shows an initial increase followed by a decrease in the phase diagram. Accordingly, we plot the normalized M_z as a function of temperature (Fig. 5c, inset), showing the non-monotonic temperature dependence, which is qualitatively consistent with our observations (Fig. 3c).

Non-collinear phases in tDB CrI_3 have also recently been reported elsewhere[12,33], though voltage control and a detailed ground-state phase diagram were not provided. Although the general existence of non-collinear phases in our study is consistent with these reports, there are a few qualitative and quantitative differences. First, an additional transition is observed at fields larger than 1 T (also seen in 4L CrI_3) in the smallest-twist-angle (reported to be around 0.5°) tDB CrI_3 sample[33]; our samples do not show such a high-field transition in small-twist-angle samples. More importantly, for all intermediate-twist-angle samples, they observe a single abrupt jump in the magnetization when external magnetic fields are applied to reverse the net magnetization of the non-collinear phase ('one-step' reversal); in contrast, we observe two abrupt changes in magnetization ('two-step' reversal). Finally, the critical twist angle up to which non-collinear phases are quantitatively observed differs between the two studies. Such distinct behaviours in different samples could result from the sensitivity of non-collinear phases and their field-dependent evolution to twist angles (given a typical accuracy of around 0.5°) and the amount of disorder/material parameters, with possible differences and effects related to lattice reconstruction[10,44] and inhomogeneity. For example, we performed micromagnetic simulations on the evolution of non-collinear states with magnetic fields and found that the choice of different material parameters can indeed change the switching behaviour from a two-step reversal to a one-step reversal (Supplementary Fig. 14 provides a detailed discussion).

The main qualitative and robust features explained by our phase diagram include the emergent non-collinear phases with finite net magnetization at intermediate twist angles (with the TA-1DW state being the most probable candidate responsible for the observations), along with the magnetic field, twist angle and non-monotonic temperature dependence. The qualitative agreement between the observations and theoretical results supports the presence of non-collinear phases in tDB CrI_3. We note, however, that quantitative differences exist, for example, in the critical twist angles for the transition between the phases (also in comparison with similar work in twisted CrI_3; refs. 12,33) (Supplementary Fig. 12) and the functional forms of anomalous temperature dependence of MOKE. These differences could arise from the sensitivity of the phase diagram to material parameters, the presence of disorder[10,34] or the trapping of experimentally observed spin configurations into metastable states.

Conclusions

We have reported electrically tunable moiré magnetism in tDB CrI_3, with emergent magnetic orders that can be interpreted by a phase diagram associated with the moiré wavelength and magnetic parameters of the sample. Our findings suggest that voltage is an effective approach to control magnetic orders and magnetic switching, suggesting that the system could have potential applications in memory and spin-logic devices. The non-trivial magnetic phases could also potentially host topological skyrmion lattices[24] and magnon networks[23], and could be probed using spatially resolved measurements. As a novel degree of freedom, the twist is applicable to a range of vdW homo-/heterobilayer magnets, including ferromagnets, antiferromagnets, multiferroics and even quantum spin liquid candidates[14,45].

Methods

Crystal growth

Single-crystal CrI_3 was synthesized using the chemical vapour transport method[46]. The Cr powder and iodine pieces were mixed in a stoichiometric ratio and loaded into a quartz tube (inner diameter, 10 mm; length, 180 mm). The quartz tube was sealed under a vacuum and then transferred to a double-temperature-zone furnace. The temperatures of the hot and cold ends of the furnace were set at 650 and 550 °C, respectively. The growth with such a temperature gradient lasted for 7 days. Finally, the furnace was shut down, and the quartz tube was naturally cooled down to room temperature. The black plate-like CrI_3 crystals can be found at the cold end of the quartz tube.

Fabrication of twisted CrI_3 and gated devices

Flakes of CrI_3 were obtained by exfoliation of the bulk material onto a silicon wafer with 285 nm oxide. The bilayers were selected by optical contrast and later confirmed by AFM and MOKE measurements. The tear-and-stack technique[13,28] was employed in this work to fabricate the tDBs. We first used a polydimethylsiloxane/polycarbonate stamp to pick up an hBN flake. Then, we carefully controlled the hBN flake to contact one part of the selected bilayer CrI_3 flake. After lifting up the stamp, the contacted part of the CrI_3 flake was torn off by the hBN layer, and the remaining part was left on the silicon wafer. Then, the remaining part on the wafer was rotated with a target twist angle θ, aligned with the separated part on the hBN flake, and picked up to form the twisted stack. Afterwards, another hBN flake was picked up such that the stacked CrI_3 layers were sandwiched between hBN and protected from degradation. Typical CrI_3 flakes before and after stacking are shown in Fig. 2a. To fabricate the back-gated device, few-layer graphene flakes were exfoliated and picked up during the stacking processes as the contact to tDB CrI_3. The stack was dropped onto prepatterned gold electrodes on a silicon wafer. The silicon oxide and bottom hBN flake act as back-gate dielectric layers. All the exfoliation and stacking operations were performed inside an argon glovebox to avoid degradation. The exposure time to air was kept below 10 min, and the fabricated sample was transferred into the measurement chamber before pumping down.

TEM characterization

To fabricate the transmission electron microscopy (TEM) samples, very thin (<5 nm) top and bottom hBN flakes were used to improve the dark-field image contrast. The holey silicon nitride support membrane can suspend the hBN/tDB and CrI_3/hBN stack for TEM imaging. The twisted sample was characterized by STEM equipped with a high-angle annular dark-field detector on a Thermo Fisher Scientific Themis Z aberration-corrected TEM instrument, which was operated at 300 kV and 0.25 nA current.

Polar MOKE microscopy

The polarization of linearly polarized light reflected from a magnetic material can be rotated by a Kerr angle θ_K, which is proportional to the magnetization of the material. In this work, the incident light is normal to the sample plane, and the MOKE is in the polar geometry, meaning that the magnetic vector being probed is perpendicular to the sample surface and parallel to the incident light. A balanced photodetector and lock-in method are used to obtain the MOKE signal[47]. The incident laser used here has a wavelength of 633 nm and a power of 5 μW. The sample is placed in a helium-flow optical cryostat with a base temperature of 6 K and magnetic field (perpendicular to the sample surface) up to 5 T. The laser is focused onto the sample surface by an objective with a spot diameter of 0.5 μm. Note that, in principle, the in-plane components of spins can emerge in twisted magnets even with perpendicular magnetic anisotropy[21]. A perpendicular field can induce canting of the in-plane spins (if any), contributing to a continuously varying MOKE background[48], which is typically subtracted and eliminated from our

MOKE signal (Supplementary Fig. 17). Therefore, we mainly focus on the out-of-plane components of spins with spin-flip transitions in this work.

Data availability

The data that support the findings of this study are available from the corresponding authors upon reasonable request.

Code availability

The computer code used in this study is available from the corresponding authors upon reasonable request.

References

1. Cao, Y. et al. Correlated insulator behaviour at half-filling in magic-angle graphene superlattices. *Nature* **556**, 80–84 (2018).
2. Cao, Y. et al. Unconventional superconductivity in magic-angle graphene superlattices. *Nature* **556**, 43–50 (2018).
3. Jin, C. et al. Observation of moiré excitons in WSe_2/WS_2 heterostructure superlattices. *Nature* **567**, 76–80 (2019).
4. Chen, G. et al. Evidence of a gate-tunable Mott insulator in a trilayer graphene moiré superlattice. *Nat. Phys.* **15**, 237–241 (2019).
5. Hunt, B. et al. Massive Dirac fermions and Hofstadter butterfly in a van der Waals heterostructure. *Science* **340**, 1427–1430 (2013).
6. Sharpe, A. L. et al. Emergent ferromagnetism near three-quarters filling in twisted bilayer graphene. *Science* **365**, 605–608 (2019).
7. Sunku, S. S. et al. Photonic crystals for nano-light in moiré graphene superlattices. *Science* **362**, 1153–1156 (2018).
8. Chen, X. et al. Moiré engineering of electronic phenomena in correlated oxides. *Nat. Phys.* **16**, 631–635 (2020).
9. Hu, G. et al. Topological polaritons and photonic magic angles in twisted α-MoO_3 bilayers. *Nature* **582**, 209–213 (2020).
10. Song, T. et al. Direct visualization of magnetic domains and moiré magnetism in twisted 2D magnets. *Science* **374**, 1140–1144 (2021).
11. Xu, Y. et al. Coexisting ferromagnetic–antiferromagnetic state in twisted bilayer CrI_3. *Nat. Nanotechnol.* **17**, 143–147 (2021).
12. Xie, H. et al. Twist engineering of the two-dimensional magnetism in double bilayer chromium triiodide homostructures. *Nat. Phys.* **18**, 30–36 (2021).
13. Cao, Y. et al. Superlattice-induced insulating states and valley-protected orbits in twisted bilayer graphene. *Phys. Rev. Lett.* **117**, 116804 (2016).
14. Burch, K. S., Mandrus, D. & Park, J. G. Magnetism in two-dimensional van der Waals materials. *Nature* **563**, 47–52 (2018).
15. Banerjee, A. et al. Neutron scattering in the proximate quantum spin liquid α-$RuCl_3$. *Science* **356**, 1055–1058 (2017).
16. Gibertini, M., Koperski, M., Morpurgo, A. F. & Novoselov, K. S. Magnetic 2D materials and heterostructures. *Nat. Nanotechnol.* **14**, 408–419 (2019).
17. Jiang, S. W., Shan, J. & Mak, K. F. Electric-field switching of two-dimensional van der Waals magnets. *Nat. Mater.* **17**, 406–410 (2018).
18. Li, T. X. et al. Pressure-controlled interlayer magnetism in atomically thin CrI_3. *Nat. Mater.* **18**, 1303–1308 (2019).
19. Deng, Y. et al. Gate-tunable room-temperature ferromagnetism in two-dimensional Fe_3GeTe_2. *Nature* **563**, 94–99 (2018).
20. Gong, C. et al. Discovery of intrinsic ferromagnetism in two-dimensional van der Waals crystals. *Nature* **546**, 265–269 (2017).
21. Hejazi, K., Luo, Z. X. & Balents, L. Noncollinear phases in moiré magnets. *Proc. Natl Acad. Sci. USA* **117**, 10721–10726 (2020).
22. Tong, Q. J., Liu, F., Xiao, J. & Yao, W. Skyrmions in the moiré of van der Waals 2D magnets. *Nano Lett.* **18**, 7194–7199 (2018).
23. Wang, C., Gao, Y., Lv, H. Y., Xu, X. D. & Xiao, D. Stacking domain wall magnons in twisted van der Waals magnets. *Phys. Rev. Lett.* **125**, 247201 (2020).
24. Akram, M. et al. Moiré skyrmions and chiral magnetic phases in twisted CrX_3 (X=I, Br, and Cl) bilayers. *Nano Lett.* **21**, 6633–6639 (2021).
25. Sivadas, N., Okamoto, S., Xu, X. D., Fennie, C. J. & Xiao, D. Stacking-dependent magnetism in bilayer CrI_3. *Nano Lett.* **18**, 7658–7664 (2018).
26. Wang, W.-G., Li, M., Hageman, S. & Chien, C. L. Electric-field-assisted switching in magnetic tunnel junctions. *Nat. Mater.* **11**, 64–68 (2012).
27. Jiang, S. W., Li, L. Z., Wang, Z. F., Mak, K. F. & Shan, J. Controlling magnetism in 2D CrI_3 by electrostatic doping. *Nat. Nanotechnol.* **13**, 549–553 (2018).
28. Kim, K. et al. Van der Waals heterostructures with high accuracy rotational alignment. *Nano Lett.* **16**, 1989–1995 (2016).
29. Wu, M., Li, Z. L., Cao, T. & Louie, S. G. Physical origin of giant excitonic and magneto-optical responses in two-dimensional ferromagnetic insulators. *Nat. Commun.* **10**, 2371 (2019).
30. Andrei, E. Y. & MacDonald, A. H. Graphene bilayers with a twist. *Nat. Mater.* **19**, 1265–1275 (2020).
31. Huang, B. et al. Layer-dependent ferromagnetism in a van der Waals crystal down to the monolayer limit. *Nature* **546**, 270–273 (2017).
32. Song, T. C. et al. Giant tunneling magnetoresistance in spin-filter van der Waals heterostructures. *Science* **360**, 1214–1218 (2018).
33. Xie, H. et al. Evidence of non-collinear spin texture in magnetic moiré superlattices. *Nat. Phys.* https://doi.org/10.1038/s41567-023-02061-z (2023).
34. Sun, Q. C. et al. Magnetic domains and domain wall pinning in atomically thin $CrBr_3$ revealed by nanoscale imaging. *Nat. Commun.* **12**, 1989 (2021).
35. Kohlhepp, J., Elmers, H. J., Cordes, S. & Gradmann, U. Power laws of magnetization in ferromagnetic monolayers and the two-dimensional Ising model. *Phys. Rev. B* **45**, 12287–12291 (1992).
36. Kim, M. et al. Micromagnetometry of two-dimensional ferromagnets. *Nat. Electron.* **2**, 457–463 (2019).
37. Huang, B. et al. Electrical control of 2D magnetism in bilayer CrI_3. *Nat. Nanotechnol.* **13**, 544–548 (2018).
38. Chiba, D., Yamanouchi, M., Matsukura, F. & Ohno, H. Electrical manipulation of magnetization reversal in a ferromagnetic semiconductor. *Science* **301**, 943–945 (2003).
39. Sivadas, N., Okamoto, S. & Xiao, D. Gate-controllable magneto-optic Kerr effect in layered collinear antiferromagnets. *Phys. Rev. Lett.* **117**, 267203 (2016).
40. Lei, C. et al. Magnetoelectric response of antiferromagnetic CrI_3 bilayers. *Nano Lett.* **21**, 1948–1954 (2021).
41. Lado, J. L. & Fernández-Rossier, J. On the origin of magnetic anisotropy in two dimensional CrI_3. *2D Mater.* **4**, 035002 (2017).
42. Rustagi, A., Solanki, A. B., Tserkovnyak, Y. & Upadhyaya, P. Coupled spin-charge dynamics in magnetic van der Waals heterostructures. *Phys. Rev. B* **102**, 094421 (2020).
43. Du, C. et al. Control and local measurement of the spin chemical potential in a magnetic insulator. *Science* **357**, 195–198 (2017).
44. Yoo, H. et al. Atomic and electronic reconstruction at the van der Waals interface in twisted bilayer graphene. *Nat. Mater.* **18**, 448–453 (2019).
45. Gong, C. & Zhang, X. Two-dimensional magnetic crystals and emergent heterostructure devices. *Science* **363**, eaav4450 (2019).
46. Liu, Y. & Petrovic, C. Three-dimensional magnetic critical behavior in CrI_3. *Phys. Rev. B* **97**, 014420 (2018).
47. Idzuchi, H. L., Allcca, A. E., Pan, X. C., Tanigaki, K. & Chen, Y. P. Increased Curie temperature and enhanced perpendicular magneto anisotropy of $Cr_2Ge_2Te_6$/NiO heterostructures. *Appl. Phys. Lett.* **115**, 232403 (2019).
48. Cai, X. et al. Atomically thin $CrCl_3$: an in-plane layered antiferromagnetic insulator. *Nano Lett.* **19**, 3993–3998 (2019).

Acknowledgements

We acknowledge partial support of the work from the US Department of Energy (DOE), Office of Science, through the Quantum Science

Center (QSC, a National Quantum Information Science Research Center) and Department of Defense (DOD) Multidisciplinary University Research Initiatives (MURI) program (FA9550-20-1-0322) for materials and device fabrication and the MOKE and TEM measurements. G.C. and Y.P.C. also acknowledge partial support from WPI-AIMR, JSPS KAKENHI Basic Science A (18H03858), New Science (18H04473 and 20H04623) and Tohoku University FRiDUO program in early stages of the research. M.M.R., A.R. and P.U. also acknowledge support from the National Science Foundation (NSF) (ECCS-1810494). Z.M. acknowledges support from the US DOE under grant DE-SC0019068 for sample synthesis. K.W. and T.T. acknowledge support from the JSPS KAKENHI (grant numbers 20H00354, 21H05233 and 23H02052) and World Premier International Research Center Initiative (WPI), MEXT, Japan.

Author contributions

G.C. and Y.P.C. conceived the project. G.C. fabricated the devices and performed the experiments, assisted by A.L.A. M.M.R., A.R. and P.U. performed the supporting theoretical analysis. X.L., G.C., L.L. and L.F. performed the TEM measurements. Y.Z. and Z.M. provided the bulk CrI_3 crystals. K.W. and T.T. provided the bulk hBN crystals. Y.P.C. and P.U. supervised the project. G.C., M.M.R., P.U. and Y.P.C. wrote the manuscript with input from all co-authors.

Competing interests

The authors declare no competing interests.

Additional information

Supplementary information The online version contains supplementary material available at https://doi.org/10.1038/s41928-023-00978-0.

Correspondence and requests for materials should be addressed to Pramey Upadhyaya or Yong P. Chen.

Peer review information *Nature Electronics* thanks the anonymous reviewers for their contribution to the peer review of this work.